THE JOURNAL OF PHYSICAL CHEMISTRY C

C: Energy Conversion and Storage; Energy and Charge Transport

Superior Photocatalytic Hydrogen Evolution Performances of WS over MoS Integrated with CdS Nanorods

Archana Byregowda, Nagaraju Kottam, Sanjay Nayak, Chandrasekhar Kothapalli Bannoth, and Sreedhara M.B.

J. Phys. Chem. C, **Just Accepted Manuscript** • DOI: 10.1021/acs.jpcc.0c03411 • Publication Date (Web): 08 Jun 2020

is published by the American Chemical Society. 1155 Sixteenth Street N.W., Washington, DC 20036

Superior Photocatalytic Hydrogen Evolution Performances of WS_2 over MoS_2 Integrated with CdS Nanorods

Byregowda Archana, [1,2] Nagaraju Kottam,[1]* Sanjay Nayak,[3] Kothapalli Bannoth Chandrasekhar,[2] and Madhenahalli Byrappa Sreedhara[3,4]

[1]Department of Chemistry, M S Ramaiah Institute of Technology (Autonomous Institute, affiliated to Visvesvaraya Technological University, Belguam), Bangalore, 560054, India

[2]Department of Chemistry, R & D Cell, Jawaharlal Nehru Technological University, Anantapuramu, 515001, India

[3]Chemistry and Physics of Materials Unit, Jawaharlal Nehru Centre for Advanced Scientific Research, Bangalore 560064, India

[4]Department of Materials and Interfaces, Weizmann Institute of Science, Rehovot, 76100, Israel

*Corresponding author

Email- nagaraju@msrit.edu, knrmsr@gmail.com, ORCID-0000-0003-0156-8012

ABSTRACT: Fabrication of noble metal-free semiconductor heterojunction composed of transition metal dichalcogenides (TMDs) and CdS is observed to be an efficient and economical photostable system for hydrogen evolution. In this report, ultrathin nanosheets of MoS_2, $Mo_{1-x}W_xS_2$ (x= 0.5 and 0.8) and WS_2 integrated with CdS nanorods; hierarchical nanocomposites have been developed to improve the efficiency and durability of CdS nanorods for H_2 generation. These nanocomposites exhibit outstanding H_2 evolution activity with notable efficiency and excellent stability. The activity of pure MoS_2, $Mo_{1-x}W_xS_2$ and WS_2 nanosheets are negligible, suggesting their co-catalytic action. The H_2 evolution activities of MoS_2-CdS, $MoWS_2$-CdS and WS_2-CdS nanocomposites have been systematically studied and compared. The highest H_2 evolution rates

of 19.2 $mmolg^{-1}h^{-1}$ was recorded for WS_2-CdS nanocomposite (9.7 $mmolg^{-1}h^{-1}$ for MoS_2-CdS), which is 35 times higher than that of pure CdS (0.53 $mmolg^{-1}h^{-1}$). The activity of these nanocomposites were notably superior in acidic medium (lactic acid sacrificial donor) than alkaline medium (Na_2S-Na_2SO_3 sacrificial donor). The apparent quantum yield of 10.19% was observed in lactic acid sacrificial electron donor medium. The rational design presented here not only substantially surges H_2 evolution rates but also reduces the photocorrosion of CdS. The possible mechanism has been investigated by analyzing the electronic band alignment of materials with respect to the vacuum level. Further, the H_2 evolution reactions were carried out under direct sunlight and in seawater to assess the performance of these nanocomposites in the practical applications.

INTRODUCTION

Solar-driven photocatalytic hydrogen production by means of water splitting is considered to be the most promising approach for clean, portable and renewable energy with high sustainability.[1-2] In order to push the water-splitting technologies towards the pragmatic applications, the discovery of visible light active, robust photocatalysts system with high efficiency is of paramount importance.[3] Since the pioneering work by Fujishima and Honda of a photoelectrochemical cell using TiO_2 supported Pt electrodes,[2, 4] numerous semiconductor photocatalyst with visible light response have been investigated.[1, 5-9] Among them, cadmium sulfide (CdS) has fostered a considerable interest for the efficient generation of H_2. Owing to superior characteristics such as excellent light-harvesting, tunable bandgap and appropriate flat band potential for water reduction, CdS emerged as the most studied and prominent candidate for water splitting.[10] The various nanostructures of CdS such as quantum dots, nanorods, and nanowires were extensively

investigated for photocatalytic H_2 evolution.[10] One dimensional (1D) CdS nanorods attained special interest due to distinctive properties such as direct pathways of charge transport along the 1D axis and high surface to volume ratios.[11] In addition, strong light trapping properties can be gained by adjusting the length scale of nanorods to the wavelength of visible light.[12] However, the investigation on pristine CdS reveled very poor photocatalytic efficiency, which was attributed to rapid recombination of photo-generated electrons, poor adsorption ability of water molecules and photo-corrosion.[10, 13] In spite of prominent progress in semiconductor-based H_2 generation, the poor photoconversion efficiencies retards the method far from practical applications. Several strategies such as bandgap engineering,[14] alterations in chemical composition[15-16], textural modification and surface sensitization have been developed in an attempt to improve the photocatalytic efficiency.[6] Amongst, the integration of light-absorbing material with proper cocatalytic surfaces, which not only effectively separate photo-generated charge carriers but also enables water adhesion and stability of the catalyst, attracted immense attention due to the synergistic effects.[13, 17-19]

Generally, noble metals such as Au and Pt are used to support the catalyst surface as cocatalyst,[20] while they are efficient due to their high cost, makes the process very expensive.[10] Two dimensional (2D) layered materials such as graphene and TMDs were demonstrated as a cost-effective and efficient cocatalyst to facilitate the development of H_2 evolution further.[13, 21-24] These Van der Wall materials can be easily shredded or chemically exfoliated into few-layer nanosheets, and they show distinct physical and chemical properties.[25-26] The ultrathin nanosheets of TMDs proved to be ideal catalytic surfaces owing copious amounts of catalytically active edge sites, superior conductivity, photo and chemical stability.[27-28] In the family of TMDs, MoS_2 and WS_2 attracted great attention as cocatalyst towards the photochemical H_2 evolution.[29-33] Both

crystallizes in a hexagonal lattice in which metal atoms sandwiched by S atoms, held together by covalent forces within the layer by van der wall forces along *c*-direction (scheme 1). The S atoms on the exposed edges in TMDs show a strong affinity towards H^+ in the solutions and facilitates the reduction of water.[28] The heterostructures of MoS_2 and WS_2 with CdS appeared to be an excellent combination for efficient catalytic activity due to suitable band alignment compared to other light-absorbing species.[34-36] MoS_2/WS_2-CdS forms a type 1 heterojunction with CdS, in which photoexcited electrons transfer from CdS to MoS_2/WS_2 nanosheets thereby reduces the recombination and increases the chances of superior photocatlytic performances.[37-38] The MoS_2, WS_2 -CdS based nanocomposites have been studied in recent days.[35, 39-44] The hydrothermally grown MoS_2 on WS_2 nanosheets decorated with CdS exhibit better catalytic activity than their pristine composites.[35] There are no cases where Mo is stoichiometrically replaced by W to systematically compare and understand H_2 evolution performances of MoS_2, WS_2 and ternary $MoWS_2$. Owing to the positive intrinsic properties, both MoS_2 and WS_2 offer efficient charge separation and a large number of catalytically active sites but differ in their band alignment with CdS. Therefore, it is worth comparing the H_2 evolution activities of MoS_2, $MoWS_2$ and WS_2 -CdS nanocomposites systematically and understand the behavior through the band alignment.

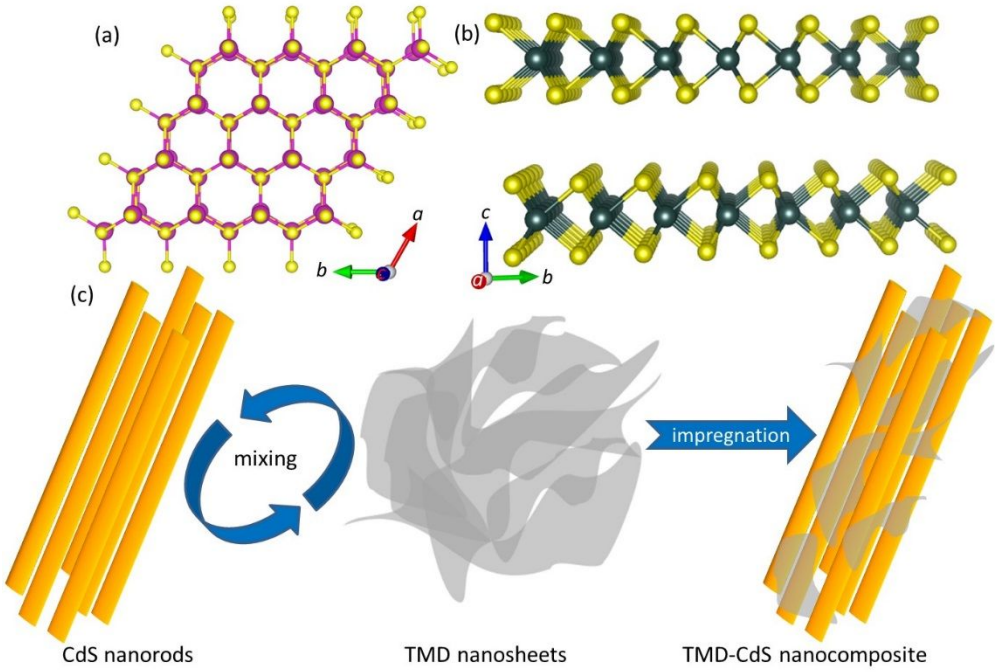

Scheme 1. (a) Crystal structure of CdS projected in (100) direction represented in ball and stick model (atom colors Cd-pink, S-yellow). (b) Crystal structure of MoS_2/WS_2 projected along (001) direction represented in ball stick model (atom colors W/Mo-green, S-yellow). (c) Schematic representation of the preparation of TMD-CdS hierarchical nanocomposites from 1D nanorods (CdS) and 2D sheets (MoS_2/WS_2).

Herein, we report the fabrication of MoS_2, $Mo_{1-x}W_xS_2$ (x= 0.5 and 0.8) and WS_2 nanosheets with CdS nanorods (*2D+1D*) hierarchical nanocomposites for photochemical H_2 generation. Single crystalline CdS nanorods and TMDs nanosheets were preferred here to reduce the bulk charge recombination aided by superior transport properties. Replacing a portion of Mo by W in MoS_2 gives rise to the ternary $MoWS_2$, and their properties would be interesting due to their stimulating chemical composition and structural modulations. The H_2 evolution performances were systematically investigated under visible light and cocatalytic activities of MoS_2 and WS_2 and ternary alloys of $MoWS_2$ were compared. Additional experiments were carried out in the

sunlight and seawater in order to evaluate the practical applicability of these nanocomposites. Detailed microscopic and spectroscopic analysis have been carried out to ascertain observed results. In addition, the positions of valence and conduction bands with respect to the vacuum level were assessed by experimentally obtained bandgap values to shed light on their band alignment and hence catalytic activity.

EXPERIMENTAL SECTION

All chemicals used for the synthesis are of high purity and purchased from commercial sources. Analytical grade $CdCl_2$. $2.5H_2O$ (Sigma-Aldrich), thiourea (SD Fine Chem Ltd, India), ethylenediamine (Merck), absolute ethanol (Merck), tungstic acid (Alfa Aesar), molybdic acid (Alfa Aesar) and were used without further purification.

Growth of CdS Nanorods. CdS nanorods with high aspect ratios were prepared through the solvothermal method. In a typical synthesis $CdCl_2$. $2.5H_2O$ (3.7 g) and thiourea (4.6 g) were dissolved in ethylenediamine (60 mL) by stirring for 15 min. The resultant solution was transferred into a 100 mL Teflon lined stainless steel autoclave and heated at 160 ℃ for 48 h. The autoclave was directly removed from the oven and cooled at ambient conditions. The yellow product was collected by filtration, then washed several times with deionized water and absolute ethanol to remove residues of the solvent and dried. As obtained product is further used to get nanocomposite photocatalyst by decorating on the cocatalyst as described below.

Synthesis of WS_2, MoS_2, $Mo_{0.5}W_{0.5}S_2$ and $Mo_{0.2}W_{0.8}S_2$ Nanosheets. The few-layer nanosheets of MoS_2, WS_2 and $Mo_{1-x}W_xS_2$ (x= 0.5 and 0.8, hereafter $MoWS_2$ for simple notation) were prepared by the solid-state method. Molybdic acid (H_2MoO_4) or tungstic acid (H_2WO_4) were ground finely with thiourea in 1:48 molar ratio using mortar and pestle. The finely ground powder

was transferred into a 15 ml alumina boat, the boat was then placed in a quartz reactor and inserted it into the horizontal furnace. The reactor was fitted with couplings and was purged with high pure N_2 at the flow rate of 15 ml/min throughout the experiment. The furnace was ramped to 500 ℃ with a rate of 5 ℃/min and hold at this temperature for 5 h. Upon the completion of the reaction, the furnace was cooled down to room temperature at the rate of 5 ℃/min down to 200 ℃ and naturally afterward. The reaction with the excess of thiourea helps to obtain the sulfur-rich environment and produces flakes with only few layers (3-4 layers). In similar experiments, the $Mo_{0.5}W_{0.5}S_2$ (0.5:0.5:48) and $Mo_{0.2}W_{0.8}S_2$ (0.2:0.8:48) nanosheets were prepared using the stoichiometric amount of H_2MoO_4 and H_2WO_4 with thiourea. The obtained products were dark grey in color and used further for the preparation of heterostructure photocatalyst.

Synthesis of MoS_2/CdS, WS_2/CdS, $Mo_{0.5}W_{0.5}S_2$/CdS and $Mo_{0.2}W_{0.8}S_2$/CdS Hierarchical Heterostructure Nanocomposites. The hierarchical nanocomposite photocatalyst comprising of few-layer nanosheets (2D) of TMDs and nanorods (1D) of CdS were prepared by the wet solution process followed by annealing. In a typical experiment $MoS_2/WS_2/MoWS_2$ and CdS were dispersed in methanol (20 mL) by sonication for 10 min. The suspension was dried on a hot plate at 70 ℃ with continuous stirring. The dried sample was transferred into the alumina boat and annealed at 200 ℃ in a horizontal tube furnace under N_2 atmosphere for 2 h. To test the effect of cocatalyst loading on the photocatalytic activity, several photocatalysts with WS_2 (1, 3, 5,10 and 20wt%), MoS_2 (1, 5 10 and 20wt%), $Mo_{0.5}W_{0.5}S_2$ (1, 3, and 5wt%) and $Mo_{0.2}W_{0.8}S_2$ (1, 3, and 5wt%) have been prepared. As prepared heterostructure composites photocatalysts were characterized and tested for H_2 evolution reaction under visible light.

Materials Characterization. Powder X-ray diffraction (XRD) patterns were recorded in a Panalytical Empyrean X-ray diffractometer in θ-2θ scan using monochromatic Cu Kα radiation

(λ = 1.5404Å). The surface morphology of pristine and nanocomposites was obtained using Field Emission Scanning Electron Microscope (FESEM) Nova NanoSEM 600 FESEM (FEI Company) equipped with an Energy Dispersive X-ray (EDX) chemical analyses system. Transmission electron microscopy (TEM) images were obtained using Tecnai G2 S-twin operated microscope (FEI) fitted with a Gatan CCD camera at an accelerating voltage of 200 kV. TEM sample was prepared by sonicating a minute quantity of the sample in ethanol and the suspension was drop cast on to the lacey carbon grid. The ultraviolet-visible (UV-Vis) diffuse reflectance spectra were collected using Perkin-Elmer Lambda 900 UV-Vis-NIR spectrometer in the diffuse reflectance mode in the range 200–1000 nm. Raman spectra were recorded with a JobinYvon LabRam HR spectrometer using a 632 nm HeNe laser in the backscattering geometry. The Raman frequency was calibrated using Si(100) 520.7 cm^{-1} signal before the measurements. X-ray photoelectron (XP) spectra were recorded using a Omicron nanotechnology spectrometer with Mg Kα X-ray source (E = 1253.6 eV).

Photocatalytic Hydrogen Generation. Hydrogen evolution experiments via splitting of water were performed in a photocatalytic cell under continuous irradiation of visible light. The components of the cell were kept stirring throughout the experiment and the evolved hydrogen was quantified using gas chromatography. In a 130 mL glass reactor, 10 mg catalyst was dispersed in 70 mL deionized water and 5 mL lactic acid has been added to the mixture as a sacrificial agent. This solution was subjected to ultra-sonication for 20 min to obtain a homogeneous mixture. The cylindrical reactor was fitted with headspace and closed with high-quality septa to ensure no leakage of evolved gases. Before the light irradiation, the reactor was de-aerated by purging with high purity Ar gas for 10 min to remove the dissolved oxygen. The reactor was positioned 5 cm away from the light source and irradiated with 400 W Xenon arc lamp (New Port, 6279NS ozone-

free) fitted with a 395 nm optical filter to cut UV portion of the light. The evolved hydrogen gas was sampled using an airtight syringe (5 mL) and analyzed by Perkin Elmer Clarus 580 GC chromatograph. The GC is furnished with a thermal conductivity detector (TCD) with 5Å molecular sieve column. The chromatogram was collected at an interval of 1 h by manually injecting the samples. To test the recyclability and photostability of the catalyst, the hydrogen evolution experiment was carried out up to 12 h by purging out the evolved H_2 in each cycle (each cycle duration was 3 h) using Ar gas. Several additional experiments were carried out by varying the components of the catalytic reactor to compare the H_2 production rates under different conditions. The experiments with varying catalyst amount were performed by keeping the other component of the reactor invariable to know the optimum amount of the catalyst for the efficient H_2 generation. The rate of H_2 evolution activity was tested with two different sacrificial reagents Na_2S-Na_2SO_3 and lactic acid independently. The pristine MoS_2, WS_2, $MoWS_2$ nanosheets and CdS nanorods were tested individually to compare with their corresponding heterostructure nanocomposite. The few photocatalytic experiments were performed under direct sunlight on the rooftop to validate the above experimental results under natural light and ambient conditions. Further, the H_2 evolution activities were checked in seawater (collected from the Arabian Sea, western cost Mangalore, India) instead of DI water, to know the stability and catalytic activity of these composites in saltwater, which is most unfavorable condition for catalysis.

The apparent quantum yield of the reaction was calculated according to the following equation

$$Q_y\,(\%) = \frac{Number\ of\ e-reacted}{Number\ of\ incident\ photons} \times 100$$

$$Q_y\,(\%) = \frac{2 \times Number\ of\ H_2\ molecules\ evolved}{Number\ of\ incident\ photons} \times 100$$

The Q*y* was measured under the same photocatalytic hydrogen evolution experimental conditions (400 W Xe lamp with 395 nm cut-off filter). The lamp spectrum and details of the AQY calculations has been described in the supplementary information.

RESULTS AND DISCUSSION

The nanosheets of layered MoS_2, WS_2 and $MoWS_2$ were obtained by solid-state reaction and CdS nanorods by solvothermal method. Scheme 1 shows the crystal structure of CdS and MoS_2/WS_2 nanosheets along the growth direction and their morphological illustration respectively. The heterostructure nanocomposites were prepared by anchoring CdS nanorods on TMD nanosheets via the impregnation method and followed by annealing (scheme 1c). Figures 1a and b show XRD patterns of MoS_2, $Mo_{0.5}W_{0.5}S_2$ and WS_2 nanosheets and CdS nanorods respectively. The diffraction patterns (in Figure 1a) were readily indexed 2H hexagonal phase of MoS_2/and or WS_2 (JCPDS 37-1492) with $P6_3$/mmc space group. The corresponding lattice constants of the 2H phase are a = 3.15 Å and c = 12.3 Å, in which Mo/W atoms are sandwiched by S atoms within the *ab* plane and held together by van der wall forces on *c* direction. The diffraction peaks at ~33°, ~40° and ~59° were corresponds to (100), (103) and (108) lattice planes of 2H MoS_2 and/or WS_2. The peak at 2θ ~14° and ~69° are from the *c*-planes of (002) and (008) respectively. The Scherrer broadening of XRD peaks was attributed to nanostructuring of materials. In particular, the weak and very broad signals of *(00l)* planes infers that the stacking of only few layers along *c* direction. The diffraction patterns of the alloy $Mo_{0.5}W_{0.5}S_2$ also show similar diffraction patterns as MoS_2/WS_2. The alloying of MoS_2/WS_2 lattice with W/Mo atoms should show the strain effects due to the difference in the ionic radii, but these atoms fit well with the lattice without any discrepancy due to less mismatch. The XRD patterns of pristine CdS (Figure 1b) show sharp

features, which implies a high degree of crystallinity of as-synthesized nanorods. All diffraction planes were indexed to hexagonal CdS of $P6_3$/mmc space group with lattice constants of a=4.141Å and c=6.720 Å (JCPDS 41-1049). The XRD patterns of the nanocomposite photocatalysts were recorded and are similar to CdS, as the cocatalyst diffraction signals are weak and are in shadow of strong CdS signals. Nevertheless, the cocatalyst loading can be seen from the color differences of the nanocomposites in the photographed images (Figure S1, *supplementary information*). As the cocatalyst loading increases, the samples appear to be dark yellow in color compared to the intense yellow color of the bare CdS.

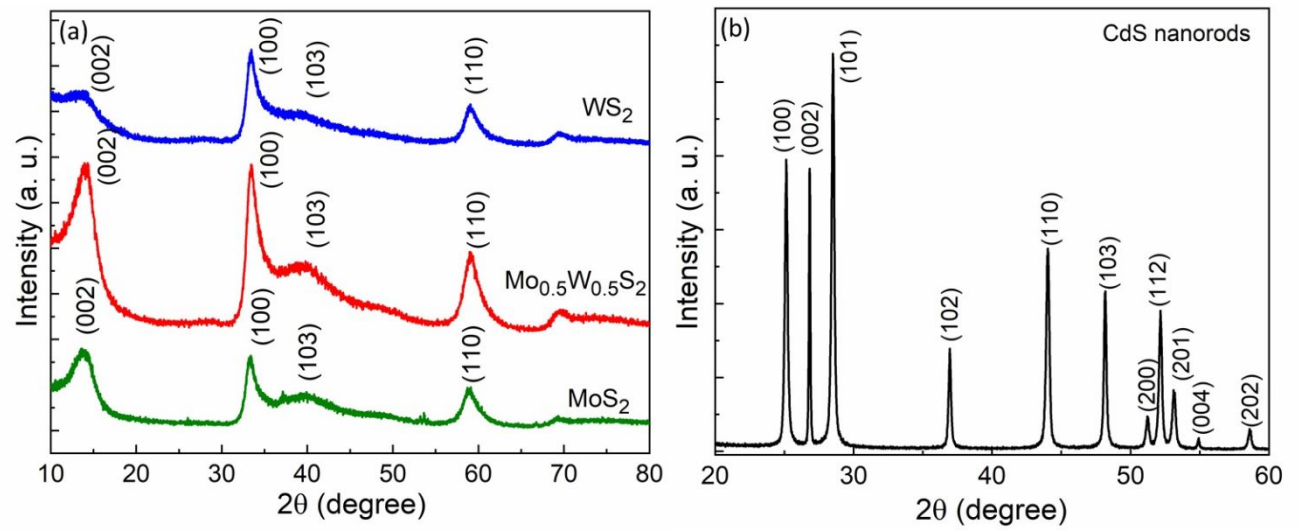

Figure 1. Powder X-ray diffraction patterns of (a) MoS_2, $Mo_{0.5}W_{0.5}S_2$ and WS_2 nanosheets (2D) prepared by solid-state reaction (b) CdS nanorods obtained by solvothermal method.

Raman spectroscopy is an effective tool to investigate the structural modulations in nanomaterials and composites. The optical phonon vibrations of bare MoS_2, WS_2, $MoWS_2$, and CdS were recorded using 532 nm laser excitation under ambient conditions (Figure S2, *SI*). The Raman

spectra of MoS_2 and WS_2 (Figure S2a) show two strong signals due to in-plane E_{2g} and out-of-plane A_{1g} optical phonon modes. The Raman modes for MoS_2 appear at 390 and 411 cm^{-1} while for WS_2, appear at 362 and 427 cm^{-1} respectively. The frequency difference between the A_{1g} and E_{2g} mode for MoS_2 is 21 cm^{-1}, which implies the MoS_2 with only few-layers stacking in *c*-direction.[45-46] The Raman spectra of ternary alloys $Mo_{1-x}W_x S_2$ (x=0.5 and 0.8) show the modes correspond to both MoS_2 and WS_2 (modes are denoted as E^1_{2g} for MoS_2 and E^2_{2g} for WS_2) infers the presence of Mo-S and W-S boding in a lattice. The alloy with the composition of $Mo_{0.5}W_{0.5}S_2$ clearly shows the overlapping of two A_{1g} phonon modes related to MoS_2 and WS_2 and could be easily deconvoluted (Figure S2). This observation confirms that ternary alloys constitute both MoS_2 and WS_2 lattices and agrees well with the reported literature.[47] The intensity of phonon modes related to MoS_2 diminishes in $Mo_{0.5}W_{0.8}S_2$ since the number of MoS_2 lattice decreases and thereby their phonon contribution. Bare CdS nanorods show two characteristic Raman bands at 305 cm^{-1} related fundamental band of a longitudinal optical phonon ((1LO) mode and the first overtone at 610 cm^{-1} (2LO) (Figure S2b) corresponding to the hexagonal lattice.[48] The strong intensity of the fundamental 1LO band indicates that the obtained nanorods are crystalline.

SEM images of pristine CdS photocatalyst displayed in Figure S3 (*SI*) reveals the nanorod morphology. The CdS nanorods exhibit definite shape and size with a width of 20 nm to 50 nm and length varies from several hundred nm to few μm. No other morphology such as nanoparticles and flakes were observed, indicating uniformity in the growth. FESEM images of as prepared WS_2-CdS heterostructure composite catalyst acquired from the different places shown in Figure 2(a-c). The CdS nanorods were randomly spread over the WS_2 nanosheets is evident from these images. The MoS_2-CdS and $MoWS_2$-CdS composites also exhibit a similar type of distribution of CdS on the co-catalyst surfaces (Figure S4 and S5, *SI*). The CdS nanorods exhibit very good

interfacial contact with the surface of the nanosheets, which certainly helps in the charge separation of photogenerated carriers during the catalytic process. The energy dispersive X-ray spectrum (EDS) of the samples clearly showed the existence of each element Cd, S, Mo, W of a particular nanocomposite respectively.

Further, the morphology and chemical components of the pristine and nanocomposite catalyst were investigated by Transmission electron microscopy (TEM) and TEM-EDS analysis. The low-magnification TEM images in Figure S6(*SI*) clearly show the nanorod morphology of CdS. The high-resolution TEM images (Figure S6d and e, *SI*) show the lattice fringes (equally spaced by 3.5 Å) along the growth direction of nanorods and are corresponds to the (*100*) Bragg planes of hexagonal CdS. The TEM images of the WS_2 cocatalyst were shown in Figure S7(*SI*), the images reveal the layered structure of the nanosheets. The lattice fringes with the spacing of 6.9 Å corresponds to the (*00l*) planes of hexagonal WS_2. The spacing of WS_2 nanosheets is a bit higher than that of bulk WS_2 (6.2 Å) indicating the less stacking and exfoliated nature of the flakes, as revealed by the XRD studies. The low and high-magnification TEM images of WS_2-CdS nanocomposites were shown in Figure 2 (d-f). The intimate contact between CdS nanorods and WS_2 nanosheets were clearly seen. The HRTEM image displayed in Figure 2e shows the lattice fringes of the CdS nanorods as well as WS_2 nanosheets clearly indicating crystallinity both the components of the nanocomposite. The intensity profiles presented in Figure 2f extracted from Figure 2e show that the lattice spacing of nanosheets (cocatalyst) and nanorods (catalyst) along the growth direction. The values correspond to (*00l*) of hexagonal WS_2 and (*100*) Bragg planes of CdS. The TEM images of the MoS_2-CdS and $MoWS_2$-CdS nanocomposites were shown in Figure S8 and S9 (*SI*) respectively. The images exhibit a similar structure and morphological signature as

observed in the case of WS_2-CdS composite. The electron diffraction (ED) patterns presented in the Figure S8c and S9b (*SI*) show clearly distinguishable diffraction spots without concentric rings,

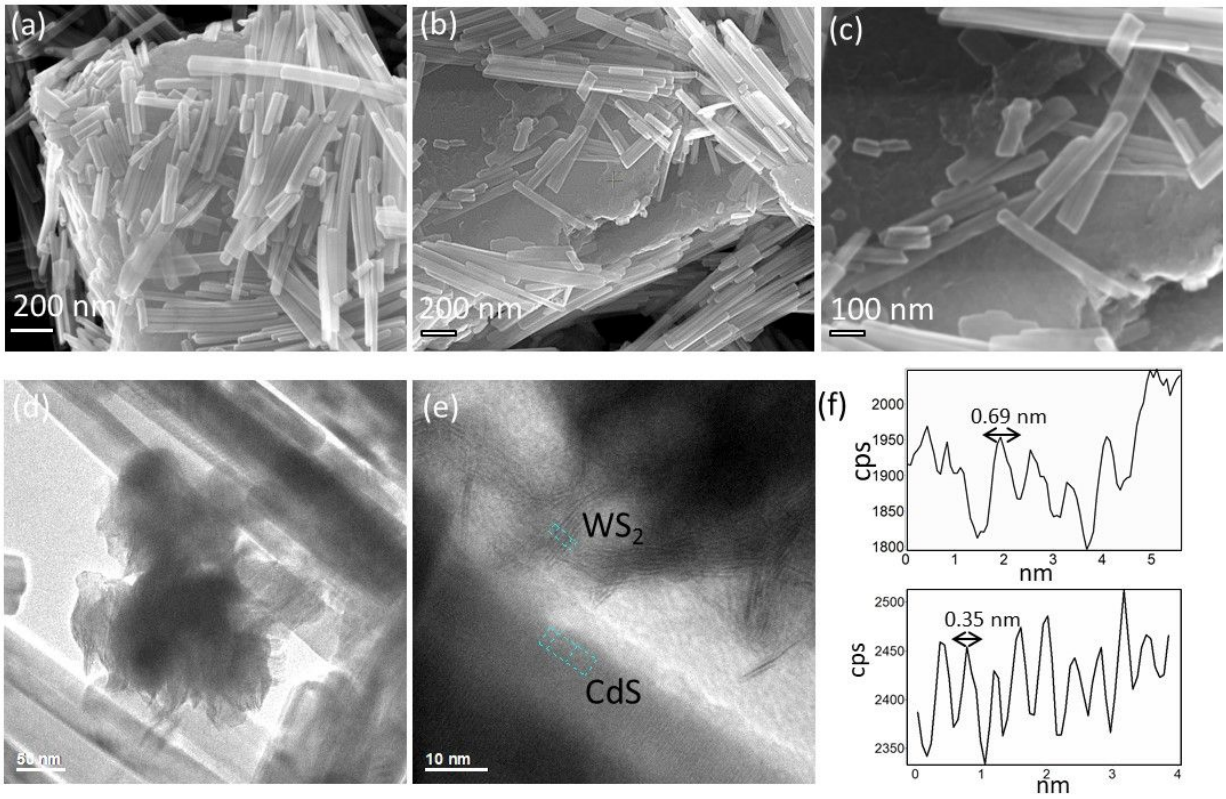

Figure 2. Plane-view FESEM images of (a-c) WS_2-CdS heterostructure composite catalyst. The CdS nanorods were spread over the WS_2 nanosheets can be clearly seen. (d) Low-magnification TEM image of WS_2-CdS heterostructure composite catalyst (e) High-resolution (HR-TEM) images of the WS_2-CdS composite catalyst at the interface of CdS nanorod and WS_2 nanosheets. (f) Intensity line profiles taken from the HRTEM image (e), the upper panel shows the lattice spacing of WS_2 nanosheets along (*00l*) direction and the lower panel is of CdS nanorod along the growth direction of the rod (marked as green boxes in the image).

confirming the single-crystalline nature of both nanostructures in the photocatalyst. In order to see the distribution of the chemical entities in the nanocomposite, TEM-EDS elemental mapping of WS_2-CdS has been acquired and shown in Figure S8 (*SI*). The EDS spectrum shows the signals

related to Cd, W and S along with C and Cu from the TEM grid. The chemical mapping images (Figure S10d-f, *SI*) display the distribution of the W, S and Cd in the composite catalyst. To probe the chemical environment and oxidation states of the components of WS_2-CdS (10wt%) composite X-ray photoelectron (XP) spectroscopy analyses was used. The XPS survey scan spectrum (Figure S11a, *SI*) shows the Cd, W and S at their standard binding energy which confirms the formation of nanocomposites. The high-resolution XP spectra for Cd 3d and S 2p (Figure S11b,c) show the features of Cd $3d_{5/2}$ and $3d_{3/2}$ at 404.6 and 411.4 eV, and S $2p_{3/2}$ and $2p_{1/2}$ at 161.45 and 162.6 respectively, which indicates divalent nature of Cd and S. The high-resolution spectrum of W 4f was very broad which may be due to the lower quantity of WS_2 in the nanocomposite.

The study of optical properties of pristine and nanocomposites are of importance to reveal the light absorption capabilities and charge transfer characteristics. The optical absorption features of as prepared nanocomposites and the pristine compounds were recorded using a UV-Vis spectrometer in diffused reflectance geometry. Figure 3 shows the UV-visible spectra in the range from 800 to 350 nm of all compounds under study. The CdS nanorods show a strong optical absorption band around ~506 nm corresponding to its optical band gap of 2.45 eV. The nanosheets of WS_2, MoS_2 and $MoWS_2$ exhibit the absorption band in the visible region around 600 to 700 nm (see inset of Figure 3a). The optical bandgaps of the nanosheets were calculated using Kubelka-Munk function and found to be 1.8, 1.6 and 1.7 eV for WS_2, MoS_2 and $MoWS_2$ respectively. The bandgap of ternary alloy $MoWS_2$ falls exactly in between MoS_2 and WS_2, this observation endorses the fact that Mo and W reside in the single lattice by the formation of alloy instead of forming two different compounds (solid solution). The nanocomposites catalysts show both the absorption bands corresponding to CdS nanorods and TMDs nanosheets. The very weaker

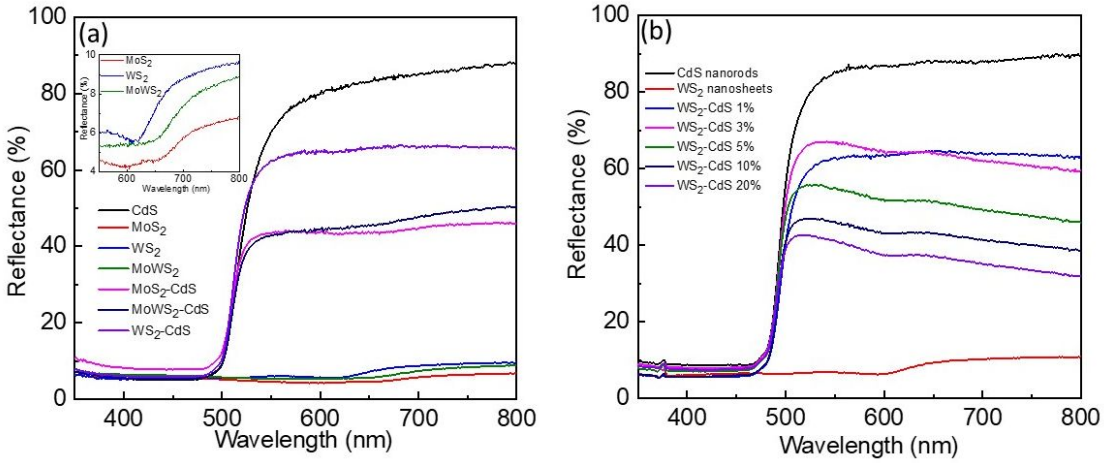

Figure 3. (a) UV-Vis Optical diffuse reflectance spectra of pristine CdS nanorods, WS_2, $MoWS_2$, MoS_2 nanosheets in comparison with $Mo_xW_{1-x}S_2$-CdS (x= 0, 0.5 and 1.0) (2D+1D) heterostructures combination (inset shows the enlarged view absorption spectra of WS_2, $MoWS_2$, MoS_2 nanosheets). (b) Comparison of diffuse reflectance spectra of WS_2-CdS (1 to 20wt%) heterostructure composites with CdS nanorods and WS_2 nanosheets.

absorption of nanosheets in the composites was attributed to small loadings of cocatalyst and strong absorption of CdS nanorods dominates the band corresponds to the nanosheets. The diffuse reflectance spectra in Figure 3b shows the absorption of WS_2-CdS nanocomposites with varying amounts of WS_2 loading with respect to CdS. The absorption band edges of both the nanostructures are clearly visible on the moderate loading of the cocatalyst. Upon decoration CdS nanorods with WS_2 (MoS_2 or $MoWS_2$) nanosheets, the reflectance in the visible region was dropped from 90% to below 60% and further drops to 40% for the 20 wt% WS_2 loading. This observation indicates the increase in visible light absorption ability of WS_2-CdS nanocomposites that may help to increase the catalytic activity. The effect of cocatalyst loading on the optical appearance of CdS also evident from the photographed images of the nanocomposites (see Figure S1, *SI*). Similar spectral features have been observed for MoS_2-CdS nanocomposites (see Figure S12, *SI*). Since CdS is a very good

luminescent semiconductor, the kinetics of photogenerated charge carriers (separation and migration) in these nanocomposites can be revealed using photoluminescence (PL) spectroscopy. Several recent studies showed that PL intensity quenches of upon integration of CdS with TMDs or graphene nanosheets.[42] The quenching of PL intensity indicates the better charge separation and lesser recombination of the charge carriers. Since PL studies of similar kinds of nanocomposites are well known, we expect akin charge separation mechanism for the composites studied here.

Sacrificial electron donor assisted photocatalytic hydrogen generation experiments were carried out under visible light (λ>395 nm) to assess the activity of the as-prepared nanocomposites. Figure 4a shows hydrogen evolution profiles of MoS_2-CdS, $MoWS_2$-CdS and WS_2-CdS nanocomposites in comparison with bare CdS with 1wt% cocatalyst loading. All the nanocomposites show notably superior catalytic activity compared to bare CdS. MoS_2-CdS, $Mo_{0.5}W_{0.5}S_2$-CdS, $Mo_{0.2}W_{0.8}S_2$-CdS and WS_2-CdS nanocomposites with 1wt% of co-catalyst loading recorded the activity of 12400, 7725,10214 and 13132 $\mu molg^{-1}$ at the end of 3 h, while bare CdS show just 1539 $\mu molg^{-1}$. The activity of CdS was observed to be approximately ten times lesser compared to the nanocomposites with 1wt% cocatalyst. The poor catalytic activity of CdS attributed to recombination of photogenerated electrons. The enhancement in photocatalytic activity of the nanocomposites is due to coherent separation and migration of photogenerated charge carriers and efficient utilization

of the electrons in the reduction of water. It is noted that surfaces of the TMDs nanosheets have a good affinity towards H^+, which further helps the migrated electron to reduce H^+ into H_2. Among the four-nanocomposite studied here, the WS_2-CdS catalyst shows the highest H_2 evolution activity

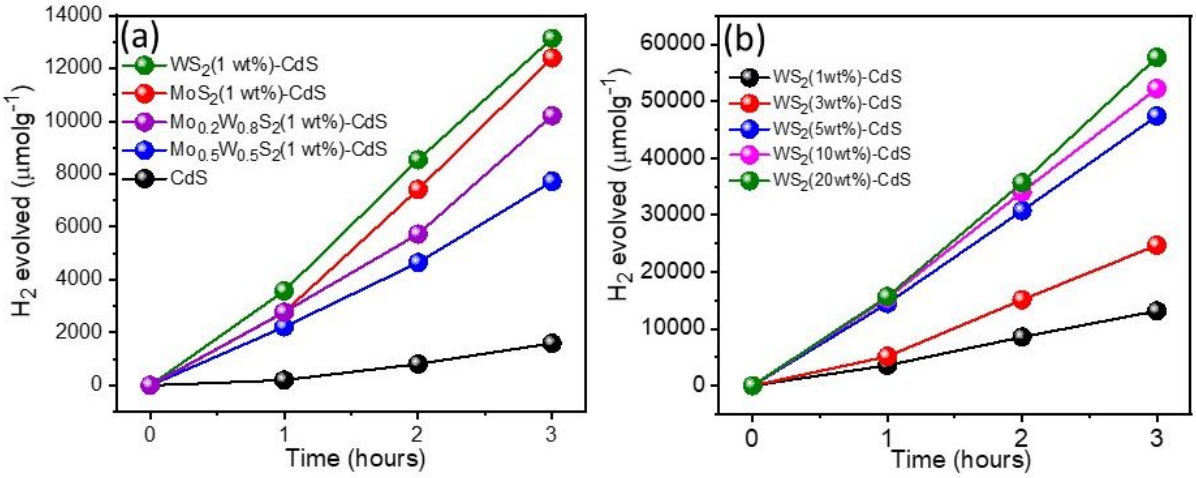

Figure 4. (a) Visible light-induced hydrogen evolution profiles by WS_2-CdS, MoS_2-CdS and $Mo_{0.5}W_{0.5}S_2$-CdS (1wt% of co-catalyst) in comparison with pristine CdS in the presence of lactic acid as hole scavenger in water. (b) Comparison of the performance of WS_2-CdS heterostructure photocatalyst for photochemical H_2 generation by varying the amount of co-catalyst (1-20wt%) under the same conditions as mentioned earlier.

(Figure 4a). In order to find the optimal amount of cocatalyst loading for the efficient generation of hydrogen, WS_2-CdS nanocomposites with the varying amount of cocatalyst were analyzed for H_2 evolution. Figure 4b shows, evolved hydrogen as a function of time for WS_2-CdS catalysts with varying amounts (1 to 20wt%) of WS_2 nanosheets. Hydrogen evolution rates sharply increase with the amount of cocatalyst from 1wt% to 5wt%, and the saturation of the catalytic activity observed after 5wt% cocatalyst loading (see Figure S13, *SI*). The increase in the hydrogen evolution rates

with the cocatalyst amount was attributed to an increase in the active catalytic sites for water reduction and quantity of charge separation. The saturation behavior of the catalytic activity (>5wt%) implies that the majority of the photogenerated carriers separated efficiently by cocatalyst and utilized for water reduction. A similar trend has been observed in the case of MoS_2-CdS nanocomposites with varying catalyst loading (see Figure S14, *SI*). WS_2-CdS shows H_2 evolution rate of 19.2 $mmolh^{-1}g^{-1}$, which is highest among all the photocatalyst prepared in this study whereas MoS_2-CdS shows the H_2 evolution rate of 9.7 $mmolh^{-1}g^{-1}$. The catalyst loading beyond 20wt% does not show much improvement in the hydrogen evolution rates. The apparent quantum yield has been calculated (see *SI*) using lamp spectra (Figure S15, *SI*) and are found to be 10.19% for WS_2-CdS and 4.8% for MoS_2-CdS respectively.

In order to test the activity of the above nanocomposites in a practical situation, photocatalytic experiments were carried out under direct sunlight (see the setup in Figure S16, *SI*). All other experimental conditions were kept the same as above to compare the obtained results. Figure 5a shows the comparison of H_2 evolution rates of WS_2-CdS (10wt%) nanocomposite catalyst under natural sunlight and xenon lamp (λ>395 nm). The photocatalyst shows H_2 evolution rates of 16.3 $mmolh^{-1}g^{-1}$ under sunlight and 17.3 $mmolh^{-1}g^{-1}$ in xenon lamp illumination after 3 h and the values are quite comparable within the experimental errors. The minor differences in the activity may be due to the intensity differences and power of the photons showered on the catalytic reactor. The above experiments show very satisfactory results and motivated us to study the stability and activity of these catalysts in various conditions for practical applicability. The catalyst activity of WS_2-CdS (10wt%) was recorded in the seawater and compared with the results of ` DI water. Figure 5b display the comparison of H_2 evolution activity of WS_2-CdS (10wt%) catalyst in DI water and seawater (collected from the Arabian sea, western coast, Mangalore, India).

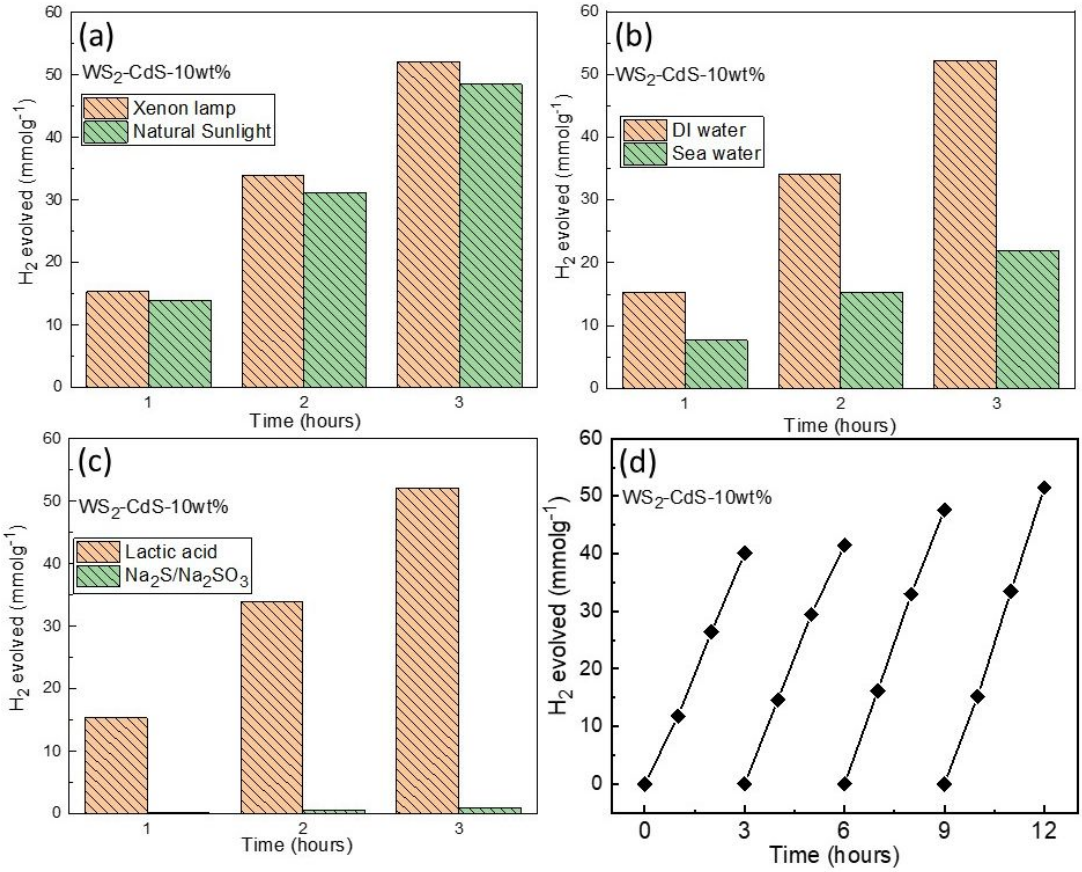

Figure 5. (a) Comparison of hydrogen evolution profiles of WS_2-CdS-10wt% (a) under direct sunlight and xenon lamp light irritation (b) in DI water and seawater in the presence of ascorbic acid as a hole scavenger. (c) In the presence of different hole scavenging agents, ascorbic acid and Na_2S-Na_2SO_3. (d) Cyclic H_2 evolution test under visible light in the presence of ascorbic acid hole scavenger in DI water, after every 3 h, the catalytic reactor was purged with Ar gas to remove evolved H_2 and the experiment was continued.

WS_2-CdS (10wt%) nanocomposite display H_2 evolution rates of 7.5 $mmolh^{-1}g^{-1}$ in the seawater whereas 17.3 $mmolh^{-1}g^{-1}$ in DI water. The activity of the catalyst in seawater reduces to its ~50% compared to DI water, which may be due to the adverse effect of salts present in the seawater. Nevertheless, the activities of these nanocomposite catalysts in the seawater are better than the activity of several similar composite catalysts in DI water reported elsewhere (Table 1).

In addition to lactic acid, the catalytic activity of the nanocomposites was tested in the presence of Na_2S-Na_2SO_3 sacrificial agents (alkaline medium). WS_2-CdS (10wt%) shows excellent activity in the presence of lactic acid, whereas almost negligible activity observed with Na_2S-Na_2SO_3 (Figure 5c). To examine the stability and durability of the photocatalyst, the experiments were repeated for four consecutive cycles (1 cycle=3 h, activity recorded at every 1 hour). After every cycle, the catalytic reactor was purged freshly with argon gas to remove the accumulated H_2 and the new experiment was run with the same catalyst. The nanocomposite catalyst shows exceptional stability and cyclability even after 12 h (Figure 5d).

The photocatalytic activity of the composites studied here are compared with similar photocatalyst reported and the results are tabulated in Table 1. The nanocomposites in the present study show satisfactory results and display notably superior catalytic activity and excellent stability under various conditions. The superior catalytic activity mainly attributed to efficient charge separation by hierarchical nanocomposite design as suggested by the earlier reports. The additional charge separation efficiency in present TMD–CdS design was driven by the crystallinity of both the component (catalyst and cocatalyst) of the heterostructure photocatalyst. The single crystalline nature of the CdS nanorods reduces the bulk charge recombination and helps the charge carriers to reach cocatalyst surface. The crystallinity of cocatalyst also plays a crucial role in engaging electrons and utilizing them efficiently in the reduction of water. It is well-known that the crystalline samples are advantageous for the photogenerated charge carriers to migrate to the surface and facilitate the reaction. Further, the excess S precursor (1:48 M:S) used during preparation TMDs leads to many unsaturated surface-active S atoms at the edge planes. These unsaturated S atoms have a strong affinity towards H^+, which further facilities catalytic reaction. In order to confirm the above stated photostability, after the cyclic test, the nanocomposite was

collected by centrifugation and analyzed using SEM, TEM and EDS. FESEM images in Figure S17 (*SI*) show that nanorods and nanosheets morphology of CdS and WS_2 are intact and are similar

Table 1. Comparison of the Activity of CdS-MoS_2 and CdS-WS_2 Based Nanocomposites for Visible Light Photocatalytic Hydrogen Evolution Reaction via Water Splitting

Nanocomposite	morphology	evolved H_2	reference no.
CdS-Au	nanospheres-quantum dots	0.6 $mmolh^{-1}g^{-1}$	20
CdS-graphene	Nanoparticles-nanosheets	1.12	24
CdS-MoS_2	nanocrystals-nanosheets	1.4 $mmolh^{-1}g^{-1}$	36
CdS-WS_2		1.9 $mmolh^{-1}g^{-1}$	
CdS-Au/MoS_2	nanorods-nanoparticles/nanosheets	7.0 $mmolh^{-1}g^{-1}$	22
CdS-graphene/MoS_2	nanoparticles-nanosheets/nanosheets	1.8 $mmolh^{-1}g^{-1}$	13
CdS-MoS_2	nanowire-nanosheets	19.14 $mmolh^{-1}g^{-1}$	32
CdS-WS_2	nanosheets-nanosheets	14.1 $mmolh^{-1}g^{-1}$	34
CdS-WS_2	nanorods-nanosheets	12.2 $mmolh^{-1}g^{-1}$	39
CdS-WS_2	nanorods-few-layer nanosheets	19.2 $mmolh^{-1}g^{-1}$	present work
CdS-$Mo_{0.5}W_{0.5}S_2$		6.12 $mmolh^{-1}g^{-1}$	
CdS-$Mo_{0.2}W_{0.8}S_2$		7.65 $mmolh^{-1}g^{-1}$	
CdS-MoS_2		9.18 $mmolh^{-1}g^{-1}$	

to the nanocomposite before the photocatalytic reaction. The EDS spectra and elemental mapping of the catalyst after the H_2 evolution reaction show the presence of all the elements Cd, S and W and their uniform distribution (Figure S18, *SI*). Further, the TEM images show the morphology of the nanocomposite is unaltered (Figure S18, *SI*). The HRTEM shows the lattice fringes spaced by 3.5 Å and 6.8 Å corresponds to CdS (100) and WS_2 (001) Bragg planes respectively. The ED pattern (Figure S19c, *SI*) shows the bright spots related to CdS and WS_2 in the composite. These results indicate the crystallinity of both the components in the nanocomposite is retained even after several reaction hours. These observations also support the claim that the crystallinity of the

composites plays a crucial role in the catalytic performance, photostability and efficiency of the photocatalyst.

In order to shed light on the better catalytic activity of WS_2-CdS nanocomposites over MoS_2-CdS composites, the adjustment of the band offset potential have been investigated and compared with CdS with respect to the vacuum level. The valence band position of CdS, MoS_2, and WS_2 wrt vacuum level are taken from the references.[49-50] The conduction band minimum values are positioned by adding experimentally obtained optical bandgap values to valence band maximum positions (see Figure 6a). From the band alignment diagram, it is clear that the band alignment of MoS_2-CdS and WS_2-CdS follow semiconductor type 1 heterojunction. Figure 6b shows the CB and VB positions of CdS, MoS_2 and WS_2 with respect to the vacuum level in comparison with the water reduction potential. The CB position of WS_2 falls just 40 meV below the CdS whereas the differences between valence band maxima and conduction CB position of the

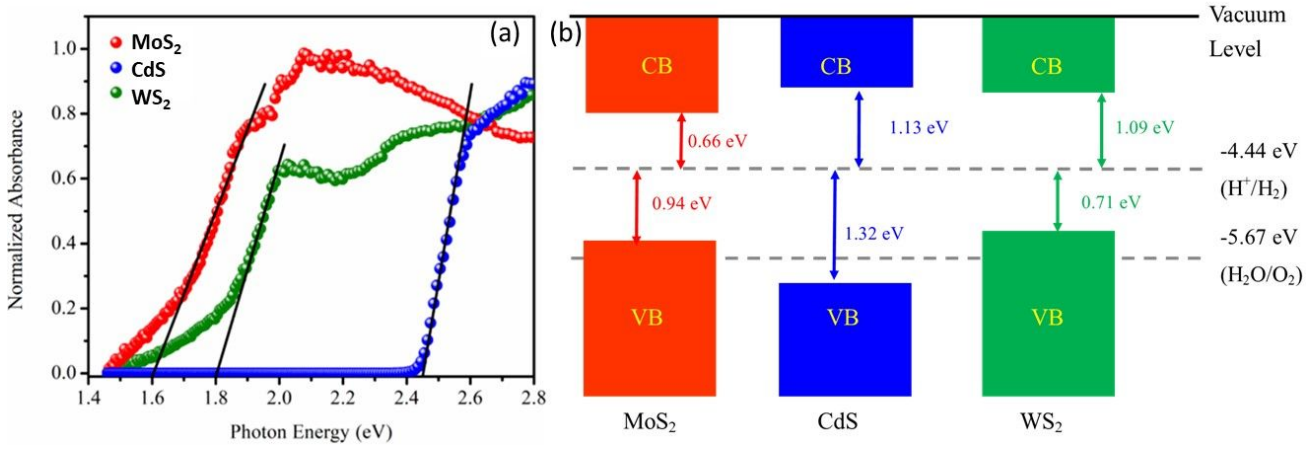

Figure 6. (a) Optical absorption spectrum showing the bandgap of MoS_2, WS_2 and CdS respectively. These values were used to determine the energy of valence band and conduction band edges with respect to vacuum level for MoS_2, WS_2 and CdS. (b) Comparision of the energy band minima of MoS_2, WS_2 and CdS with respect to vacuum level.

MoS_2 much deeper (470 meV) with respect to CB of CdS. The migration of photo-generated electron from CdS to WS_2 is more facile than the CdS to MoS_2 due lower CB offset energy of WS_2 with CdS. The differences in the band alignment of MoS_2 and WS_2 with respect to CdS explains the observed differences in the H_2 evolution rates and efficiency of the WS_2-CdS catalyst over MoS_2-CdS.

CONCLUSIONS

The noble metal-free CdS based heterostructure nanocomposites with TMDs were successfully synthesized via facile chemical routes. The characterization reveals that both the components of the nanocomposites are highly crystalline and CdS nanorods are decorated finely on TMDs nanosheets. The well-designed robust photocatalytic systems show excellent catalytic activity for efficient generation of H_2 and photostability. By tuning the composition from MoS_2 to WS_2 and optimizing other conditions, the nanocomposite with WS_2 showed notably superior catalytic activity than MoS_2 and ternary $MoWS_2$. The H_2 evolution rates WS_2-CdS nanocomposite in the presence of lactic acid as a sacrificial agent were higher compared to reported Pt-CdS, graphene-CdS systems. Though the charge separation plays a crucial role, the crystallinity of nanocomposites, active S edge atoms and appropriate band offsets induced synergetic effects are responsible for improved photocatalytic efficiency. The band offset between WS_2 and CdS is minimum and more coherent than the MoS_2 and CdS, which explains the observed superior catalytic activity of WS_2-CdS composite. The comparative study presented here would guide to the more rational use of WS_2 cocatalyst and progressive appeal for efficient and economical solar energy directed photocatalytic H_2 production.

Associated content

Supplementary figures and AQY calculations – Raman spectra, SEM and TEM images, Electron diffraction, chemical mapping of nanocomposites, reflectance spectra etc.

Acknowledgments

Authors thank Dr. Anand K Roy for his insights, help and fruitful discussions. Jawaharlal Nehru Centre for Advanced Scientific Research, Bangalore (JNCASR) and Indian Institute of Science (IISC) for facilities. Authors also acknowledges the management of M S Ramaiah Institute of Technology, Bangalore for their support.

REFERENCES

1. Chen, X.; Shen, S.; Guo, L.; Mao, S. S. Semiconductor-Based Photocatalytic Hydrogen Generation. *Chem. Rev.* **2010**, *110*, 6503-6570.

2. Fujishima, A.; Rao, T. N.; Tryk, D. A. Titanium Dioxide Photocatalysis. *J. Photochem. Photobiol., C* **2000**, *1*, 1-21.

3. Fan, W.; Zhang, Q.; Wang, Y. Semiconductor-Based Nanocomposites for Photocatalytic H2 Production and Co2 Conversion. *Phys. Chem. Chem. Phys* **2013**, *15*, 2632-2649.

4. Fujishima, A.; Honda, K. Electrochemical Photolysis of Water at a Semiconductor Electrode. *Nature* **1972**, *238*, 37-38.

5. Corredor, J.; Rivero, M. J.; Rangel, C. M.; Gloaguen, F.; Ortiz, I. Comprehensive Review and Future Perspectives on the Photocatalytic Hydrogen Production. *J. Chem. Technol. Biotechnol.* **2019**, *94*, 3049-3063.

6. Ge, M.; Cai, J.; Iocozzia, J.; Cao, C.; Huang, J.; Zhang, X.; Shen, J.; Wang, S.; Zhang, S.; Zhang, K-Q.; et al. A Review of Tio2 Nanostructured Catalysts for Sustainable H2 Generation. *Int. J. Hydrogen Energy* **2017**, *42*, 8418-8449.

7. Archana, B.; Manjunath, K.; Nagaraju, G.; Chandra Sekhar, K. B.; Kottam, N. Enhanced Photocatalytic Hydrogen Generation and Photostability of Zno Nanoparticles Obtained Via Green Synthesis. *Int. J. Hydrogen Energy* **2017**, *42*, 5125-5131.

8. Kudo, A.; Miseki, Y. Heterogeneous Photocatalyst Materials for Water Splitting. *Chem. Soc. Rev.* **2009**, *38*, 253-278.

9. Kamat, P. V. Meeting the Clean Energy Demand: Nanostructure Architectures for Solar Energy Conversion. *J. Phys. Chem. C* **2007**, *111*, 2834-2860.

10. Cheng, L.; Xiang, Q.; Liao, Y.; Zhang, H. Cds-Based Photocatalysts. *Energy Environ. Sci.* **2018**, *11*, 1362-1391.

11. Bartnik, A. C.; Efros, A. L.; Koh, W. K.; Murray, C. B.; Wise, F. W. Electronic States and Optical Properties of Pbse Nanorods and Nanowires. *Phys. Rev. B* **2010**, *82*, 195313.

12. Jang, J. S.; Joshi, U. A.; Lee, J. S. Solvothermal Synthesis of Cds Nanowires for Photocatalytic Hydrogen and Electricity Production. *J. Phys. Chem. C* **2007**, *111*, 13280-13287.

13. Chang, K.; Mei, Z.; Wang, T.; Kang, Q.; Ouyang, S.; Ye, J. Mos2/Graphene Cocatalyst for Efficient Photocatalytic H2 Evolution under Visible Light Irradiation. *ACS Nano* **2014**, *8*, 7078-7087.

14. Kouser, S.; Lingampalli, S. R.; Chithaiah, P.; Roy, A.; Saha, S.; Waghmare, U. V.; Rao, C. N. R. Extraordinary Changes in the Electronic Structure and Properties of Cds and Zns by Anionic Substitution: Cosubstitution of P and Cl in Place of S. *Angew. Chem. Int. Ed.* **2015**, *54*, 8149-8153.

15. Roy, A.; Singh, A.; Aravindh, S. A.; Servottam, S.; Waghmare, U. V.; Rao, C. N. R. Structural Features and Her Activity of Cadmium Phosphohalides. *Angew. Chem. Int. Ed.* **2019**, *58*, 6926-6931.

16. Roy, A.; Chhetri, M.; Prasad, S.; Waghmare, U. V.; Rao, C. N. R. Unique Features of the Photocatalytic Reduction of H2o and Co2 by New Catalysts Based on the Analogues of Cds, Cd4p2x3 (X = Cl, Br, I). *ACS Appl. Mater. Interfaces* **2018**, *10*, 2526-2536.

17. Sun, Z.; Zheng, H.; Li, J.; Du, P. Extraordinarily Efficient Photocatalytic Hydrogen Evolution in Water Using Semiconductor Nanorods Integrated with Crystalline Ni2p Cocatalysts. *Energy Environ. Sci.* **2015**, *8*, 2668-2676.

18. Zhao, Z.; Sun, Y.; Dong, F. Graphitic Carbon Nitride Based Nanocomposites: A Review. *Nanoscale* **2015**, *7*, 15-37.

19. Moniz, S. J. A.; Shevlin, S. A.; Martin, D. J.; Guo, Z.-X.; Tang, J. Visible-Light Driven Heterojunction Photocatalysts for Water Splitting – a Critical Review. *Energy Environ. Sci.* **2015**, *8*, 731-759.

20. Kuang, P.-Y.; Zheng, P.-X.; Liu, Z.-Q.; Lei, J.-L.; Wu, H.; Li, N.; Ma, T.-Y. Embedding Au Quantum Dots in Rimous Cadmium Sulfide Nanospheres for Enhanced Photocatalytic Hydrogen Evolution. *Small* **2016**, *12*, 6735-6744.

21. Xiang, Q.; Yu, J. Graphene-Based Photocatalysts for Hydrogen Generation. *J. Phys. Chem. Lett.* **2013**, *4*, 753-759.

22. Chava, R. K.; Do, J. Y.; Kang, M. Smart Hybridization of Au Coupled Cds Nanorods with Few Layered Mos2 Nanosheets for High Performance Photocatalytic Hydrogen Evolution Reaction. *ACS Sustainable Chem. Eng.* **2018**, *6*, 6445-6457.

23. Bar-Ziv, R.; Ranjan, P.; Lavie, A.; Jain, A.; Garai, S.; Bar Hen, A.; Popovitz-Biro, R.; Tenne, R.; Arenal, R.; Ramasubramaniam, A.; et al. Au-Mos2 Hybrids as Hydrogen Evolution Electrocatalysts. *ACS Appl. Energy Mater.* **2019**, *2*, 6043-6050.

24. Li, Q.; Guo, B.; Yu, J.; Ran, J.; Zhang, B.; Yan, H.; Gong, J. R. Highly Efficient Visible-Light-Driven Photocatalytic Hydrogen Production of Cds-Cluster-Decorated Graphene Nanosheets. *J. Am. Chem. Soc.* **2011**, *133*, 10878-10884.

25. Nicolosi, V.; Chhowalla, M.; Kanatzidis, M. G.; Strano, M. S.; Coleman, J. N. Liquid Exfoliation of Layered Materials. *Science* **2013**, *340*, 1226419.

26. Hu, Z.; Wang, L.; Zhang, K.; Wang, J.; Cheng, F.; Tao, Z.; Chen, J. Mos2 Nanoflowers with Expanded Interlayers as High-Performance Anodes for Sodium-Ion Batteries. *Angew. Chem. Int. Ed.* **2014**, *53*, 12794-12798.

27. Jaramillo, T. F.; Jørgensen, K. P.; Bonde, J.; Nielsen, J. H.; Horch, S.; Chorkendorff, I. Identification of Active Edge Sites for Electrochemical H₂ Evolution from Mos₂ Nanocatalysts. *Science* **2007**, *317*, 100-102.

28. Voiry, D.; Yang, J.; Chhowalla, M. Recent Strategies for Improving the Catalytic Activity of 2d Tmd Nanosheets toward the Hydrogen Evolution Reaction. *Adv. Mater.* **2016**, *28*, 6197-6206.

29. Maitra, U.; Gupta, U.; De, M.; Datta, R.; Govindaraj, A.; Rao, C. N. R. Highly Effective Visible-Light-Induced H2 Generation by Single-Layer 1t-Mos2 and a Nanocomposite of Few-Layer 2h-Mos2 with Heavily Nitrogenated Graphene. *Angew. Chem. Int. Ed.* **2013**, *52*, 13057-13061.

30. Kumar, D. P.; Song, M. I.; Hong, S.; Kim, E. H.; Gopannagari, M.; Reddy, D. A.; Kim, T. K. Optimization of Active Sites of Mos2 Nanosheets Using Nonmetal Doping and Exfoliation into

Few Layers on Cds Nanorods for Enhanced Photocatalytic Hydrogen Production. *ACS Sustainable Chem. Eng.* **2017**, *5*, 7651-7658.

31. Zhang, S.; Yang, H.; Gao, H.; Cao, R.; Huang, J.; Xu, X. One-Pot Synthesis of Cds Irregular Nanospheres Hybridized with Oxygen-Incorporated Defect-Rich Mos2 Ultrathin Nanosheets for Efficient Photocatalytic Hydrogen Evolution. *ACS Appl. Mater. Interfaces* **2017**, *9*, 23635-23646.

32. Xiang, Q.; Cheng, F.; Lang, D. Hierarchical Layered Ws2/Graphene-Modified Cds Nanorods for Efficient Photocatalytic Hydrogen Evolution. *ChemSusChem* **2016**, *9*, 996-1002.

33. He, J.; Chen, L.; Wang, F.; Liu, Y.; Chen, P.; Au, C.-T.; Yin, S.-F. Cds Nanowires Decorated with Ultrathin Mos2 Nanosheets as an Efficient Photocatalyst for Hydrogen Evolution. *ChemSusChem* **2016**, *9*, 624-630.

34. Zhang, K.; Fujitsuka, M.; Du, Y.; Majima, T. 2d/2d Heterostructured Cds/Ws2 with Efficient Charge Separation Improving H2 Evolution under Visible Light Irradiation. *ACS Appl. Mater. Interfaces* **2018**, *10*, 20458-20466.

35. Reddy, D. A.; Park, H.; Ma, R.; Kumar, D. P.; Lim, M.; Kim, T. K. Heterostructured Ws2-Mos2 Ultrathin Nanosheets Integrated on Cds Nanorods to Promote Charge Separation and Migration and Improve Solar-Driven Photocatalytic Hydrogen Evolution. *ChemSusChem* **2017**, *10*, 1563-1570.

36. Chen, J.; Wu, X.-J.; Yin, L.; Li, B.; Hong, X.; Fan, Z.; Chen, B.; Xue, C.; Zhang, H. One-Pot Synthesis of Cds Nanocrystals Hybridized with Single-Layer Transition-Metal Dichalcogenide Nanosheets for Efficient Photocatalytic Hydrogen Evolution. *Angew. Chem. Int. Ed.* **2015**, *54*, 1210-1214.

37. Min, Y.; He, G.; Xu, Q.; Chen, Y. Dual-Functional Mos2 Sheet-Modified Cds Branch-Like Heterostructures with Enhanced Photostability and Photocatalytic Activity. *J. Mater. Chem. A* **2014**, *2*, 2578-2584.

38. Yang, Y.; Zhang, Y.; Fang, Z.; Zhang, L.; Zheng, Z.; Wang, Z.; Feng, W.; Weng, S.; Zhang, S.; Liu, P. Simultaneous Realization of Enhanced Photoactivity and Promoted Photostability by Multilayered Mos2 Coating on Cds Nanowire Structure Via Compact Coating Methodology. *ACS Appl. Mater. Interfaces* **2017**, *9*, 6950-6958.

39. He, J.; Chen, L.; Yi, Z.-Q.; Au, C.-T.; Yin, S.-F. Cds Nanorods Coupled with Ws2 Nanosheets for Enhanced Photocatalytic Hydrogen Evolution Activity. *Ind. Eng. Chem. Res.* **2016**, *55*, 8327-8333.

40. Yang, M.-Q.; Han, C.; Xu, Y.-J. Insight into the Effect of Highly Dispersed Mos2 Versus Layer-Structured Mos2 on the Photocorrosion and Photoactivity of Cds in Graphene–Cds–Mos2 Composites. *J. Phys. Chem. C* **2015**, *119*, 27234-27246.

41. Yin, X.-L.; He, G.-Y.; Sun, B.; Jiang, W.-J.; Xue, D.-J.; Xia, A.-D.; Wan, L.-J.; Hu, J.-S. Rational Design and Electron Transfer Kinetics of Mos2/Cds Nanodots-on-Nanorods for Efficient Visible-Light-Driven Hydrogen Generation. *Nano Energy* **2016**, *28*, 319-329.

42. Yin, X.-L.; Li, L.-L.; Jiang, W.-J.; Zhang, Y.; Zhang, X.; Wan, L.-J.; Hu, J.-S. Mos2/Cds Nanosheets-on-Nanorod Heterostructure for Highly Efficient Photocatalytic H2 Generation under Visible Light Irradiation. *ACS Appl. Mater. Interfaces* **2016**, *8*, 15258-15266.

43. Zhang, L.; Yan, Z.; Chen, X.; Yu, M.; Liu, F.; Cheng, F.; Chen, J. Facile Synthesis of Amorphous Mosx–Fe Anchored on Zr-Mofs Towards Efficient and Stable Electrocatalytic Hydrogen Evolution. *Chem. Commun.* **2020**, *56*, 2763-2766.

44. Xu, D.; Xu, P.; Zhu, Y.; Peng, W.; Li, Y.; Zhang, G.; Zhang, F.; Mallouk, T. E.; Fan, X. High Yield Exfoliation of Ws2 Crystals into 1–2 Layer Semiconducting Nanosheets and Efficient Photocatalytic Hydrogen Evolution from Ws2/Cds Nanorod Composites. *ACS Appl. Mater. Interfaces* **2018**, *10*, 2810-2818.

45. Li, H.; Zhang, Q.; Yap, C. C. R.; Tay, B. K.; Edwin, T. H. T.; Olivier, A.; Baillargeat, D. From Bulk to Monolayer Mos2: Evolution of Raman Scattering. *Adv. Funct. Mater.* **2012**, *22*, 1385-1390.

46. Lee, C.; Yan, H.; Brus, L. E.; Heinz, T. F.; Hone, J.; Ryu, S. Anomalous Lattice Vibrations of Single- and Few-Layer Mos2. *ACS Nano* **2010**, *4*, 2695-2700.

47. Kim, J.-S., et al. High Pressure Raman Study of Layered Mo0.5w0.5s2ternary Compound. *2D Mater.* **2016**, *3*, 025003.

48. Phuruangrat, A.; Thongtem, T.; Thongtem, S. Characterisation of One-Dimensional Cds Nanorods Synthesised by Solvothermal Method. *J. Exp. Nanosci.* **2009**, *4*, 47-54.

49. Kang, J.; Tongay, S.; Zhou, J.; Li, J.; Wu, J. Band Offsets and Heterostructures of Two-Dimensional Semiconductors. *Appl. Phys. Lett.* **2013**, *102*, 012111.

50. He, G. Z., Y.; He, Q. Mos2/Cds Heterostructure for Enhanced Photoelectrochemical Performance under Visible Light. *Catalysts* **2019,** , 379.

TABLE OF CONTENT (TOC)